Showcasing research from BasCat – UniCat BASF JointLab, Technische Universität Berlin, Germany.

Boosting the performance of Ni/Al$_2$O$_3$ for the reverse water gas shift reaction through formation of CuNi nanoalloys

Supported nickel can be used as highly active catalyst for the reverse Water Gas Shift reaction, forming carbon monoxide and water from carbon dioxide and hydrogen. However, nickel tends to reduce carbon monoxide even further to methane, especially at low temperature. Supported copper catalysts are highly selective to carbon monoxide, but the catalytic activity decreases rapidly. The fusion of nickel and copper into a stable alloy is an excellent strategy to suppress methane formation and enhance carbon monoxide yield, combining the activity and stability of nickel with the selectivity of copper.

The authors thank Roma Palermo and Martin Palaminuta for their original artwork used as back cover image.

As featured in:

See Raoul Naumann d'Alnoncourt *et al.*, *Catal. Sci. Technol.*, 2022, **12**, 474.

ROYAL SOCIETY OF CHEMISTRY

rsc.li/catalysis

PAPER

Boosting the performance of Ni/Al₂O₃ for the reverse water gas shift reaction through formation of CuNi nanoalloys†

Esteban Gioria, [ID] [a] Piyush Ingale, [ID] [a] Felix Pohl, [a] Raoul Naumann d'Alnoncourt, [ID] *[a] Arne Thomas [ID] [b] and Frank Rosowski[ac]

Ni supported on alumina is extensively employed as a catalyst for the reverse water gas shift reaction. However, the formation of inactive Ni aluminates and the high selectivity to methane affects the performance of these catalysts, especially at low reaction temperatures. In this study, Cu is employed as an effective enhancer of the catalytic performance, promoting the reducibility of Ni, and suppressing methane production through the formation of stable CuNi nanoalloys. The synergy between both metals suppresses consecutive hydrogenation, reaching conversions close to equilibrium and 100% selectivity to carbon monoxide. At 500 °C, the CO yield of the Cu₂₅Ni₇₅/Al₂O₃ catalyst was twice that of Ni/Al₂O₃, with only half the hydrogen consumption. The formation of CuNi nanoalloys was confirmed by HAADF STEM–EDS, without segregation in monometallic phases even after 30 h time on stream. Similarly, Cu₅₀Ni₅₀/Al₂O₃ remained alloyed after the reaction. However, the catalytic activity decreased due to sintering, in agreement with a higher Cu content. This effect was significantly more pronounced for Cu₇₅Ni₂₅/Al₂O₃ and Cu/Al₂O₃, with formation of large particles and consequent loss of active surface area.

Introduction

Carbon monoxide is of great importance in the chemical and petrochemical industries since it is employed as a building block to produce higher-value products. The H_2/CO mixture, known as synthesis gas or syngas, is the raw material in the production of alcohols and synthetic fuels through the Fischer–Tropsch process.[1–4] At a commercial scale, the steam reforming of natural gas remains the preferred synthesis route and Ni has been employed as the key active site in supported reforming catalysts since their first industrial applications.[5,6] Nevertheless, the use of carbon dioxide as a feedstock carbon-containing molecule has gained a lot of attention in the last few decades. Carbon dioxide is one of the main by-products of the chemical industry, and its hydrogenation employing hydrogen obtained by green methods is a potential pathway towards a circular economy and the development of more sustainable processes.[7–11]

The chemical conversion of carbon dioxide to carbon monoxide *via* the reverse water gas shift (rWGS) reaction is an endothermic process (eqn (1)). This reaction requires temperatures higher than 700 °C in order to activate the thermodynamically stable CO_2 molecule and reach economically feasible conversions.[7,12] However, when the reaction takes place at lower temperatures, methane formation through the Sabatier reaction is favoured due to the exothermic nature of this side-reaction (eqn (2)):

$$CO_2 + H_2 \rightarrow CO + H_2O \quad \Delta H_R^0 = 41 \text{ kJ mol}^{-1} \quad (1)$$

$$CO_2 + 4H_2 \rightarrow CH_4 + 2H_2O \quad \Delta H_R^0 = -165 \text{ kJ mol}^{-1} \quad (2)$$

At a commercial scale, $Cu/ZnO/Al_2O_3$ and $FeCrCuO_x$ catalysts are employed due to their efficiency.[13–15] However, Cu-based catalysts suffer from deactivation due to excessive sintering at high reaction temperatures.[16,17] Therefore, highly active, selective, and stable catalysts are required to produce carbon monoxide that are consecutively applied in the Fischer Tropsch process, suppressing methane formation.

A vast number of metal combinations have been tested for the rWGS reaction. Noble metals are highly active and selective; however, their scarcity and high cost make their large-scale application unfeasible. Thus, the use of non-noble transition metals such as Ni, Co, Fe, Cu and Mo is of great interest.[18–21] Among them, Ni catalysts have shown remarkably high activity

[a] *BasCat – UniCat BASF JointLab, Technische Universität Berlin, Berlin 10623, Germany. E-mail: r.naumann@bascat.tu-berlin.de*
[b] *Functional Materials, Department of Chemistry, Technische Universität Berlin, Berlin 10623, Germany*
[c] *BASF SE, Process Research and Chemical Engineering, Ludwigshafen 67056, Germany*
† Electronic supplementary information (ESI) available. See DOI: 10.1039/d1cy01585k

and stability even at relatively low reaction temperatures. However, high selectivity to methane *via* consecutive hydrogenation of carbon monoxide poses a challenge. In addition, Ni catalysts supported on alumina can form inactive species of low reducibility like Ni aluminates.[22,23]

The incorporation of a second metal is an effective way to tune the electronic properties of the active sites and several promoters have been proposed as an alternative to enhance the selectivity to carbon monoxide of Ni-based catalysts.[24–26] Indeed, the benefits of bimetallic catalysts for the rWGS reaction are mostly related to higher metal dispersion, enhanced CO_2 activation and improved CO desorption.[27–29]

Hence, one of the most promising alternatives is the use of Cu, due to its inherent high selectivity to carbon monoxide.[30,31] Based on temperature programmed desorption studies, Liu *et al.* have shown that Cu significantly promotes the selectivity to carbon monoxide of supported Ni catalysts on alumina.[32] This effect was attributed to the lower hydrogen adsorption capacity of Cu compared with Ni and thus suppression of consecutive carbon monoxide hydrogenation to methane. More recently, experimental results and theoretical simulations showed that Cu–Ni catalysts have an outstanding performance compared to their monometallic counterparts, related to the formation of alloyed nanostructures.[33–37] However, low thermal stability and excessive sintering limit their application at relatively high reaction temperatures.[38,39]

Surprisingly, studies based on transmission electron microscopy and energy-dispersive X-ray spectroscopy that corroborate the formation of CuNi alloyed nanoparticles in the rWGS reaction are still scarce. In the present study, a set of five different mono- and bimetallic Cu–Ni catalysts supported on alumina were tested in the reverse water gas shift reaction in the range of 500–600 °C. The incorporation of Cu into Ni catalysts suppresses methane formation through the formation of bimetallic nanoalloys, enhancing carbon monoxide yield and decreasing hydrogen consumption. The use of alumina as a support improves the stability of bimetallic nanoparticles due to the strong interaction with the support through Ni aluminate species. In addition, Cu–Ni alloyed nanostructures were stable after 30 h time on stream, without segregation in monometallic phases.

Therefore, we believe that our work brings new insights in terms of copper-promoted nickel-based catalysts. The formation of stable bimetallic CuNi alloys suppresses methanation and thus enhances the performance in terms of CO yield and hydrogen consumption. To the best of our knowledge, this is the first report where CuNi/Al$_2$O$_3$ catalysts applied for rWGS are characterized by STEM–EDS, clarifying the role of nanoalloys without a doubt.

Experimental

Synthesis of Cu–Ni catalysts

The catalysts were prepared by incipient wetness impregnation. Bimetallic catalysts were prepared by co-impregnation. In a typical protocol, 1 g of the γ-alumina support was impregnated

with 0.95 ml of Cu and/or Ni nitrate solution containing the desired amount of metallic precursors. The nominal metal loading was fixed to 5% wt. Metal nitrates were chosen as a precursor because of their low cost, good solubility in water and facile decomposition.[40] The catalysts were dried at 120 °C overnight and calcined at 500 °C for 4 h employing a heating rate of 10 K min^{-1} and a 200 ml min^{-1} flow of 21% O$_2$/N$_2$. The catalysts were named Cu$_{xx}$Ni$_{yy}$/Al$_2$O$_3$, where *xx/yy* refers to the Cu/Ni mass ratio. Cu(NO$_3$)$_2$·3H$_2$O, Ni(NO$_3$)·6H$_2$O (99.99%, Sigma-Aldrich, Germany) and H$_2$O HPLC grade (Honeywell Riedel-de-Haën, Germany) were used as received without any further purification.

Characterization

Thermal gravimetric analysis (TGA) was carried out using an STA 409 apparatus (Linseis) employing 25 mg of the sample at a temperature range of 25–900 °C, with a heating rate of 10 K min^{-1} and a flow rate of 20 mL min^{-1} of 20% O$_2$/N$_2$.

Elemental analysis (carbon, nitrogen, hydrogen and sulphur) was performed on a Thermo FlashEA 1112 organic elemental analyzer by a dynamic flash combustion method operating at 1020 °C.

X-ray diffractograms of the powder samples were acquired in Bragg–Brentano geometry on a Rigaku SmartLab 3 kW with Cu Kα radiation (λ = 1.54 Å) over an angular range from 10° to 80° and a scan rate of 2° min^{-1}.

The chemical composition of the mono- and bimetallic catalysts was determined by inductively coupled plasma–atomic emission spectroscopy (ICP–AES) on a Jobin Yvon Horiba ULTIMA 2000 spectrometer. The samples were digested in *aqua regia* HCl/HNO$_3$ 3:1 v/v (nitric acid 69%, SUPRA-Qualität ROTIPURAN® and hydrochloric acid 30%, SUPRA-Qualität ROTIPURAN®) and the mean of three reproducible independent experiments is reported.

Temperature programmed reduction experiments were carried out using a BelCat-II equipped with a thermal conductivity detector (TCD). For each measurement, 250 mg of sample was heated up to 900 °C employing a heating rate of 6 K min^{-1} in 5% H$_2$/N$_2$ with a total flow of 50 mL min^{-1}. Operating conditions were optimized following the recommendations reported by Monti *et al.*[41]

Nitrogen sorption analysis was carried out using a Quadrasorb SI (Quantachrome GmbH & Co. KG Odelzhausen, Germany) after degassing the samples for 12 h at 150 °C. The surface area was determined using the Brunauer–Emmett–Teller (BET) method, and the corresponding pore size distribution was obtained by non-local density functional theory (NLDFT).

X-ray photoelectron spectroscopy (XPS) was carried out using a Thermo Fisher Scientific ESCALAB 250Xi. An Al-Kα X-ray source (1486.6 eV) was employed for the analysis, with a pass energy of 200 eV for a survey, and 50 eV for high-resolution spectra. The samples were activated following a similar reduction treatment to that of the catalytic test and stored under an inert atmosphere in the glovebox (MBraun

LABmaster Pro). Before measurements, the catalysts were briefly in contact with air during sample holding. The analysis of the spectra was done using CasaXPS software. The C1s peak of adventitious carbon at 284.6 eV was taken as a reference of charge-shift correction for the measured spectra.

The morphology, composition and size distribution of the supported nanoparticles were analysed by high-angle annular dark-field-scanning transmission electron microscopy (HAADF-STEM) and energy dispersive X-ray spectroscopy (EDS) elemental mapping using a Thermo Scientific Talos F200X microscope operated at an accelerating voltage of 200 kV. The microscope is equipped with a SuperX EDX detector system. Samples were prepared by dipping the lacey carbon 400-mesh gold grids (Plano GmbH) into the powder sample. STEM–EDS mappings show the net intensities of the corresponding elements with a post-filtering Gaussian blur of 1.1 sigma.

Catalytic activity: CO_2 hydrogenation

The catalytic experiments were carried out at atmospheric pressure and in a set-up designed by Integrated Lab Solutions (ILS, Berlin, Germany). 25 mg of each sample (pressed and sieved between 100 and 200 μm) was loaded into a quartz-tube reactor. The activation of each sample was performed *in situ* for 60 min at 500 °C in 100 mL min^{-1} of 10% H_2/He with a heating rate of 10 K min^{-1}. The reactor was purged with a 100 mL min^{-1} He flow after activation treatment for 10 min. Afterwards the reactant mixture (40 mL min^{-1} CO_2 : 40 mL min^{-1} H_2 : 20 mL min^{-1} N_2) was introduced into the reactor, and the reaction temperature was modified in a ramping up–ramping down cycle at 500–550–600 °C. The resulting gas hourly space velocity (GHSV) was 240 000 mL g^{-1} h^{-1}.

The effluent gas stream was analysed using an online gas chromatograph (Agilent 7890A) equipped with a flame ionization detector and a thermal conductivity detector. The carbon dioxide conversion (X_{CO_2}), carbon monoxide selectivity (S_{CO}), methane selectivity (S_{CH_4}) and space–time yield of carbon monoxide (STY_{CO}) were defined as:

$$X_{CO_2} = \left(\frac{[CO_2]^{in} - [CO_2]^{out}}{[CO_2]^{in}} \right) \times 100$$

$$S_{CO} = \left(\frac{[CO]^{out}}{[CO]^{out} + [CH_4]^{out}} \right) \times 100$$

$$S_{CH_4} = \left(\frac{[CH_4]^{out}}{[CO]^{out} + [CH_4]^{out}} \right) \times 100$$

$$STY_{CO} \left(mol\ h^{-1}\ g_{metal}^{-1} \right) = \frac{X_{CO_2}\ S_{CO}\ F_{CO_2}}{w_{CuNi}}$$

where F_{CO_2} is the molar flow of carbon dioxide and w_{CuNi} is the mass amount of Cu and/or Ni in the sample.

In addition, hydrogen consumption was calculated based on the CO and CH_4 formation for each catalyst.

Results and discussion

Calcination process

Thermogravimetric analysis (TGA) of the impregnated catalysts was performed under analogous conditions to the calcination treatment as described in the Experimental section and is shown in Fig. S1.† Three different stages could be observed: the first one at 100 °C is related to the dehydration through evaporation of physisorbed water; the second and third one in the range of 215–260 °C and 360–410 °C respectively, are related to the decomposition of the nitrates by loss of hydration water and formation of gas products.[42–45] The TGA of the second stage suggested that the temperature decomposition of the mixed salts follows a linear correlation with the Cu/Ni ratio, without the influence of the second metal (Fig. S2†).

To have a clear comprehension of the decomposition process of the metallic nitrates on alumina, TG-MS analysis was performed for $Cu_{50}Ni_{50}/Al_2O_3$ (Fig. S3†). The dehydration process ($m/z = 18$; H_2O) follows a two step process: the first one around 100 °C is related to physisorbed water; and the second one at 200 °C is related to the loss of structural water of the nitrates. Regarding the nitrate decomposition, only NO was detected ($m/z = 30$), with the first decomposition step at 180 °C, followed by the second one at 280 °C and the third one at 350 °C.[46–48]

In addition, elemental analysis was performed for the impregnated (before calcination) and calcined samples. In all cases, the impregnated catalysts showed a nitrogen content close to the theoretical, corresponding to the metallic nitrates deposited on alumina (Table S1†). In contrast, there was no evidence of nitrogen content for the calcined samples. Thus, the complete thermal decomposition of the metallic precursors after the calcination treatment could be confirmed.

Crystalline phases before and after activation

The crystalline phases in both calcined and reduced catalysts were characterized by powder X-ray diffraction (XRD) as described above. For the sake of comparison, the alumina support was also included. As seen from Fig. 1, all the samples present a broad peak at 37.5°, together with the peaks at 46° and 67° which are typical of the spinel-type phase of γ-alumina.[49,50] Since Cu and Ni aluminates are also of spinel-type structure, it is difficult to distinguish them between the crystalline phases of the support.[51–53]

Fig. 1a shows the diffractograms of the calcined catalysts. There is no evidence of either Cu or Ni oxidized species. This could be related to the presence of finely dispersed nanometric metallic oxides that cannot be detected, but also to metallic spinel species that overlap the crystalline support.[54–57] However, for the Cu/Al_2O_3 catalyst, two peaks at 2θ 35.6° and 38.7° were observed, related to the diffractions
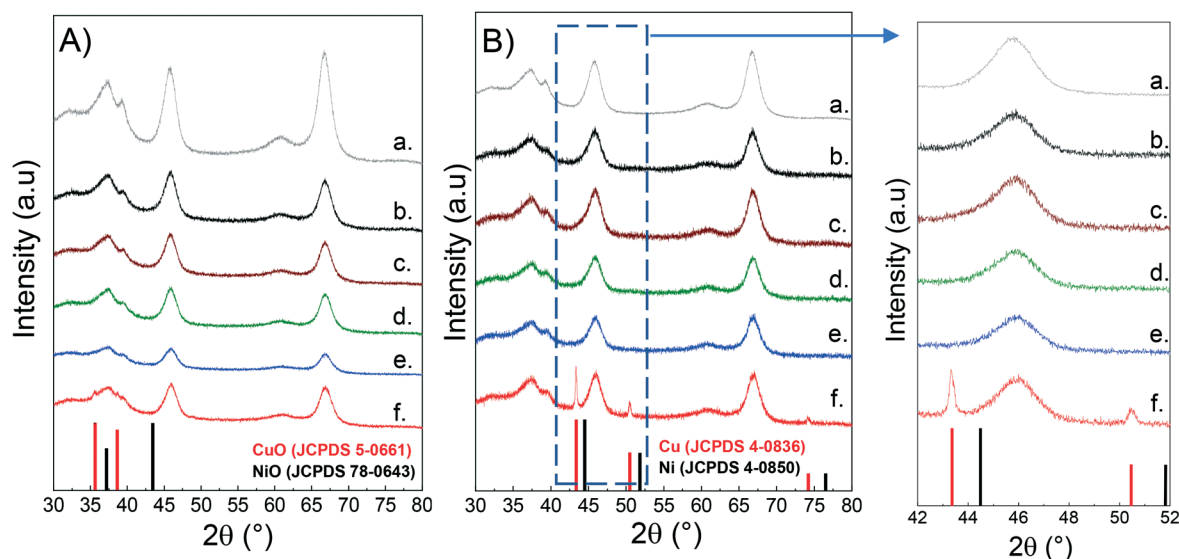
476 | *Catal. Sci. Technol.*, 2022, **12**, 474–487

This journal is © The Royal Society of Chemistry 2022

Fig. 1 XRD of CuNi/Al_2O_3 catalysts: A) calcined; B) reduced; a) Al_2O_3; b) Ni/Al_2O_3; c) $Cu_{25}Ni_{75}$/Al_2O_3; d) $Cu_{50}Ni_{50}$/Al_2O_3; e) $Cu_{75}Ni_{25}$/Al_2O_3; f) Cu/Al_2O_3.

of the (111) and (200) planes of the CuO monoclinic structure (JCPDS 5-0661).[58]

Fig. 1b shows the diffractograms of the reduced catalysts after activation in 10% H_2 at 500 °C for 1 hour. In the monometallic Cu/Al_2O_3 catalyst, it can be clearly seen that Cu oxide was successfully reduced to metallic Cu (2θ: 43.29° (111), 50.43° (200) and 74.13° (220) (JCPDS 04-0836)).[59,60] The absence of diffraction peaks for Ni/Al_2O_3 can be rationalised either by the formation of nanosized Ni nanoparticles well below the XRD detection limit and/or incomplete reduction of Ni aluminates.

Surprisingly, for the bimetallic catalysts there is no evidence of either metallic Cu or Ni. Thus, it can be inferred that Ni addition to Cu catalysts promotes the formation of small and dispersed CuNi nanoparticles, non-detectable by XRD.[61] This was later confirmed by H_2-TPR and STEM–EDS studies.

Reducibility of supported catalysts

The reducibility of supported metal catalysts strongly depends on the particle size, oxidation state, and metal–support and metal–metal interactions.[62–65] Fig. 2 shows the temperature programmed reduction (H_2-TPR) profiles of both monometallic and bimetallic CuNi/Al_2O_3 catalysts. The Cu/Al_2O_3 catalyst exhibits a sharp reduction event at 244 °C with a shoulder at 219 °C, characteristic of the reduction of dispersed CuO nanoparticles weakly bonded to the surface.[66,67]

The Ni/Al_2O_3 catalyst shows broad reduction events at higher temperatures. It is reported that under certain synthesis conditions, *e.g.* calcination temperatures higher that 500 °C and metal loading below 10%, Ni nitrate decomposes forming a spinel structure with alumina.[68–71] The absence of a reduction peak at 400 °C related to NiO and

the reduction at high temperature indicates the presence of $NiAl_2O_4$ spinel-type species.[72–74]

Whether with Al_2O_3 or within the $NiAl_2O_4$ structure, Ni^{2+} strongly interacts within the framework. The first reduction event located at 631 °C is related to Ni_{oc}^{2+} (Ni^{2+} in an octahedral geometry, defined as Ni^{2+} ions that are not completely integrated as a spinel-type structure but in strong interaction with the support). Meanwhile, the second one at 796 °C is related to Ni_T^{2+} (Ni^{2+} in a tetrahedral geometry, forming nickel aluminate of spinel-type structure).[72,75–77]
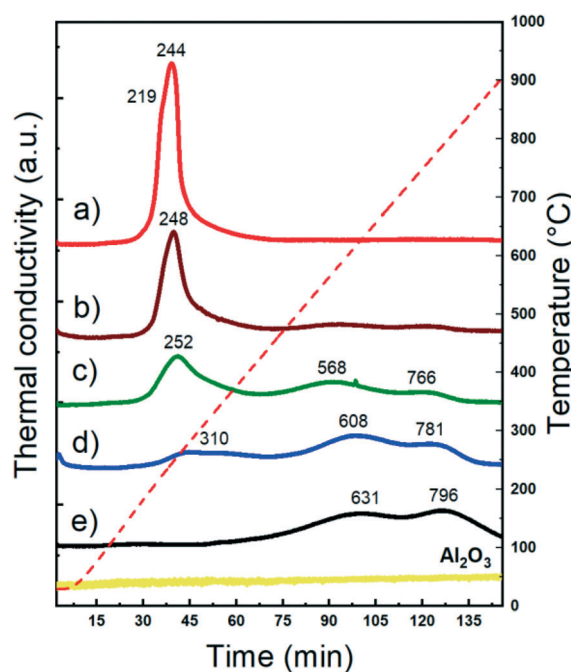

Fig. 2 H_2-TPR studies of CuNi/Al_2O_3 catalysts: a) Cu/Al_2O_3; b) $Cu_{75}Ni_{25}$/Al_2O_3; c) $Cu_{50}Ni_{50}$/Al_2O_3; d) $Cu_{25}Ni_{75}$/Al_2O_3; e) Ni/Al_2O_3.

This journal is © The Royal Society of Chemistry 2022

Catal. Sci. Technol., 2022, **12**, 474–487 | **477**

Therefore, in agreement with the H_2-TPR profiles, Ni is present as Ni^{2+} in strong interaction with the support in the calcined samples containing Ni.

Bimetallic catalysts exhibited different reduction profiles than their monometallic counterparts. The reduction events are located between the temperatures of the monometallic ones, which clearly suggests the synergy between CuO and Ni^{2+} species and thus particles in close proximity.[70,78] It is already reported that Cu promotes the reducibility of Ni-based catalysts. This can be ascribed to two main contributions: i) the enhancement of the Ni reducibility due to H_2 spillover produced from Cu and ii) a cooperative effect between both metals through the introduction of Cu to the Ni phase, reducing the interaction between Ni^{2+} and the support, and enhancing its reducibility. Indeed, from TPR it is seen that when the Cu content increased, the effect in promoting the reducibility of Ni become more pronounced.[32,33,36,79,80]

Table S2† shows the hydrogen consumption of the different catalysts after reduction at 500 °C. For Ni/Al$_2$O$_3$, 500 °C leads to a reduction degree of 13%. As expected, the reduction degree increases with the Cu content. A H_2-TPR study of the calcined alumina was also performed. As expected for non-reducible supports, no hydrogen consumption was detected.

Specific surface area and porosity

Table 1 shows the surface area, total pore volume and metal composition of the different catalysts after activation in 10% H_2 at 500 °C for 1 hour. The alumina support (untreated and after calcination) was included for comparative purposes. The chemical analysis performed by ICP showed that the desired Cu/Ni ratio and nominal metal loading were achieved.

Fig. S4† shows the nitrogen sorption isotherms and the pore size distribution. For both alumina and supported CuNi catalysts, the adsorption–desorption branches present the characteristic H1 type hysteresis of a mesoporous type IV isotherm, according to the IUPAC classification.[81] The pore size distribution showed a bimodal distribution with the main peak at 4.78 nm and a second one centred at 7.47 nm. The total pore volume decreased after impregnation,

calcination and activation from 0.950 cm^3 g^{-1} to a mean value of 0.402 cm^3 g^{-1}. However, the calcined support showed a pore volume of 0.453 cm^3 g^{-1}. Thus, the deposition of metallic species by incipient wetness impregnation does not significantly affect the textural properties of the support, without pore blockage.

Oxidation states in the near-surface region

X-ray photoelectron spectroscopy (XPS) analysis was performed to study the chemical state and the surface composition of the mono- and bimetallic catalysts after activation in 10% H_2 at 500 °C for 1 hour. The samples were stored under an inert atmosphere in the glovebox and briefly in contact with air during sample holding prior to measurements.

Fig. 3a shows the spectra for the Cu 2p region. The two major peaks corresponding to Cu^0 2p$_{1/2}$ and 2p$_{3/2}$ are located at 952.6 eV and 932.7 eV, respectively. In addition, Cu^{2+} was detected with peaks at 956.4 eV and 935.8 eV corresponding to Cu^{2+} 2p$_{1/2}$ and 2p$_{3/2}$, respectively.[82,83] The satellite components at 943 eV are generated through the O 2p to Cu 3d charge transfer effect in CuO.[84,85] The presence of CuO is related to the air contact during sample preparation. As expected, the intensity decreases with decreasing the Cu content.

By XRD, metallic Cu could be detected only for the Cu/Al$_2$O$_3$ catalyst. Thus, it is inferred that small and dispersed nanoparticles were formed in bimetallic CuNi catalysts, not detectable by XRD. This was later confirmed by STEM–EDS, showing the formation of CuNi alloyed structures.

Fig. 3b shows the spectra for the Ni 2p region. Only for Ni/Al$_2$O$_3$, corresponding to the catalyst with the higher Ni content, a small peak at 852.5 eV related to Ni^0 2p$_{3/2}$ could be detected.[86] Furthermore, XPS showed that only 9% of the Ni content is reduced, in agreement with the reduction degree of 13% at 500 °C determined by H_2-TPR in Ni/Al$_2$O$_3$.

In the case of the bimetallic CuNi/Al$_2$O$_3$ catalysts, reduced Ni could not be detected. This is related to the low Ni content (less than 3.5%) and the small fraction of Ni^0 in comparison with Ni^{2+} species, making the detection by XPS difficult.[34,87] In addition, the effect of passivation during sample holding prior to measurements should be considered.[71,88,89]

Table 1 Surface area and metal composition of the catalysts

Sample code	BET surface[a] area (m^2 g^{-1})	Total pore volume[b] (cm^3 g^{-1})	Cu content[c] (%)	Ni content[c] (%)	Total metal content (%)	Cu/Ni ratio (%)
Cu/Al$_2$O$_3$	181	0.397	4.96	—	4.96	100/0
Cu$_{75}$Ni$_{25}$/Al$_2$O$_3$	185	0.411	3.54	1.17	4.71	75/25
Cu$_{50}$Ni$_{50}$/Al$_2$O$_3$	184	0.400	2.24	2.25	4.49	49/51
Cu$_{25}$Ni$_{75}$/Al$_2$O$_3$	181	0.401	1.10	3.21	4.31	26/74
Ni/Al$_2$O$_3$	182	0.401	—	4.94	4.94	0/100
Al$_2$O$_3$ (calcined)	199	0.453	—	—	—	—
Al$_2$O$_3$ (untreated)	222	0.950	—	—	—	—

[a] Determined by BET equation. [b] Obtained by non-local density functional theory (NLDF). [c] Determined by ICP.

478 | *Catal. Sci. Technol.*, 2022, **12**, 474–487

This journal is © The Royal Society of Chemistry 2022
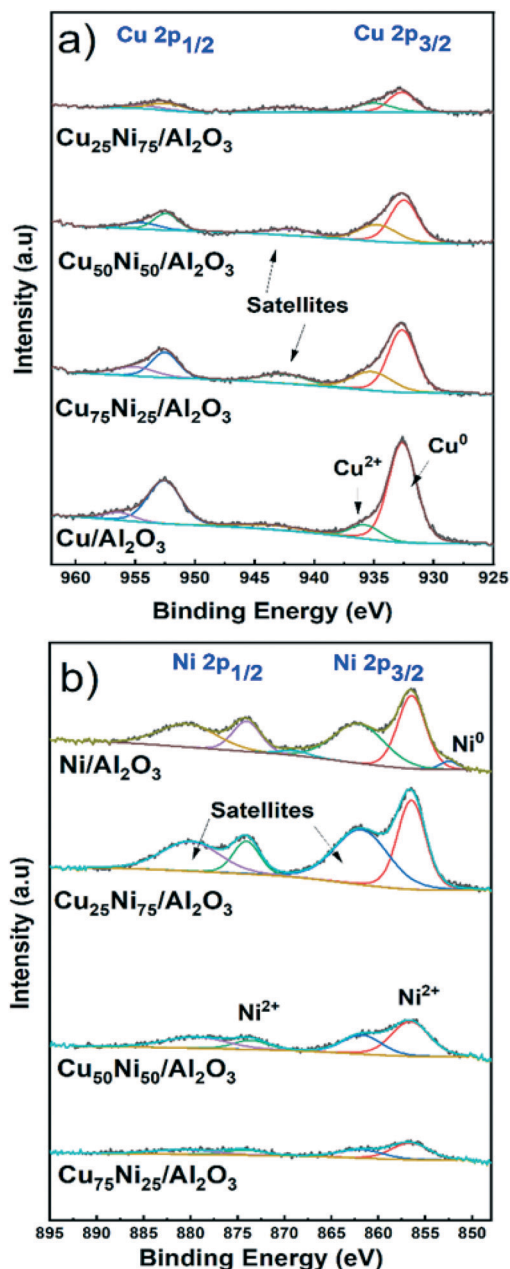
Fig. 3 XPS spectra of the reduced catalysts. a) Cu 2p and b) Ni 2p regions.

Fig. 3b shows the two major peaks corresponding to Ni^{2+} $2p_{1/2}$ and $2p_{3/2}$, located at 873.9 eV and 856.6 eV, respectively. In addition, satellites features are located at 880.4 eV and 862.3 eV. Similarly, the satellite features are generated through the O 2p to Ni 3d charge transfer effect in Ni^{2+} species.[87,90] The absence of peak splitting in the range 854–858 eV characteristic of NiO, and the high binding energy value are indicative of Ni^{2+} species in strong interaction with the support.[91–95] Thus, Ni^{2+} is well dispersed forming spinel structures of type $NiAl_2O_4$ in all Ni-containing catalysts. Therefore, the partial reduction at 500 °C formed well distributed and small metallic nanoparticles supported on

highly dispersed $NiAl_2O_4$. This is in agreement with the XRD and H_2-TPR results and later confirmed by STEM–EDS.

Table S3† shows the Cu/Ni atomic ratio determined by XPS analysis. In all cases, the atomic ratio is close to the bulk composition determined by ICP. However, for both $Cu_{75}Ni_{25}/Al_2O_3$ and $Cu_{50}Ni_{50}/Al_2O_3$, the surface Cu content is slightly higher. Meanwhile, $Cu_{25}Ni_{75}/Al_2O_3$ showed a slight Ni enrichment, in comparison with the bulk composition.

Catalytic performance in CO_2 hydrogenation

Fig. 4 shows the initial catalytic performance of the mono- and bimetallic catalysts. The evolution of the carbon dioxide conversion, selectivity to carbon monoxide and space–time yield during the 30 h time on stream can be seen in Fig. S5.† During the catalytic tests, only methane and carbon monoxide were detected as products. Hydrogen consumption was calculated based on the CO and CH_4 formation for each catalyst (Fig. S6†).

Considering the thermodynamic equilibrium and the reaction conditions (P = 1 atm; CO_2 : H_2 = 1 : 1), an equimolar CO : CH_4 product composition is reached at 530 °C.[96] A higher temperature favours the reverse water gas shift reaction and promotes carbon monoxide production. Meanwhile, a lower temperature favours methane formation.[19,22]

For Ni/Al_2O_3, CO_2 conversion reached values of 28%, 32% and 36% at 500 °C, 550 °C and 600 °C, respectively. Meanwhile, the selectivity to carbon monoxide reached values of 49%, 65% and 81% at 500 °C, 550 °C and 600 °C, respectively. In addition, no deactivation process was observed during the time on stream (Fig. S5a†). Notably, it could be observed that during the ramping down, the selectivity to carbon monoxide is increased compared with the initial one (57% *vs.* 49% at 500 °C and 67% *vs.* 65% at 550 °C, respectively, Fig. S5b†). This can be related to the continuous formation of metallic Ni sites from the reduction of the $NiAl_2O_4$ spinel, as can be inferred from the H_2-TPR results. As a drawback, Ni/Al_2O_3 showed a higher hydrogen consumption, related to its inherent high activity and trend to form not only carbon monoxide but also methane (Fig. S6†).

In contrast, the Cu/Al_2O_3 catalyst showed the lowest conversion compared with the other catalysts, and a quick deactivation during the time on stream, especially at 600 °C (Fig. S5a†). This could be related to its low thermal stability and thus, rapid deactivation due to sintering.[39,97,98] Therefore, the active surface area decreases over time, as was later confirmed by STEM–EDS. Regarding the selectivity, the Cu catalyst formed carbon monoxide as the only product.

Bimetallic $Cu_{75}Ni_{25}/Al_2O_3$ and $Cu_{50}Ni_{50}/Al_2O_3$ showed an intermediate catalytic performance. For both catalysts, carbon dioxide conversion values led between the corresponding to the monometallic ones, as can be seen in Fig. 4a. Moreover, the addition of Cu to the Ni-based catalyst drastically improved the selectivity to carbon monoxide, suppressing methane formation (Fig. 4b). As the main
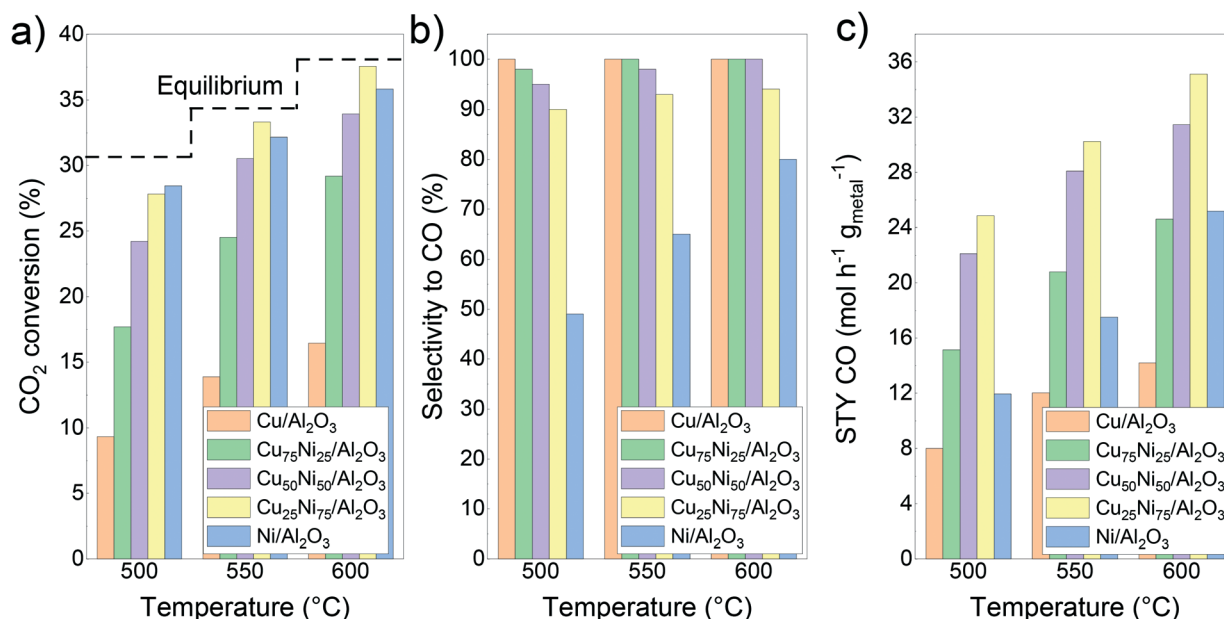
This journal is © The Royal Society of Chemistry 2022

Catal. Sci. Technol., 2022, **12**, 474–487 | **479**

Fig. 4 Catalytic performance of the $CuNi/Al_2O_3$ catalysts: a) CO_2 conversion; b) CO selectivity; c) space–time yield of carbon monoxide.

disadvantage, a clear deactivation could be observed during the time on stream, especially at 600 °C (Fig. S5a†).

In comparison to Ni/Al_2O_3, both $Cu_{75}Ni_{25}/Al_2O_3$ and $Cu_{50}Ni_{50}/Al_2O_3$ showed a higher space–time yield of carbon monoxide, as can be seen in Fig. 4c. However, the clear deactivation at 600 °C leads to lower values during the ramping down of temperature (Fig. S5†).

In comparison with the other mono- and bimetallic formulations, $Cu_{25}Ni_{75}/Al_2O_3$ showed the best performance (Fig. 4). In fact, the carbon dioxide conversion reached values close to the equilibrium. However, the conversion decreases during the ramping down (Fig. S5†), probably attributed to partial sintering of the active sites. Likewise for $Cu_{75}Ni_{25}/Al_2O_3$ and $Cu_{50}Ni_{50}/Al_2O_3$, the presence of Cu inhibited methane formation. Thus, the $Cu_{25}Ni_{75}/Al_2O_3$ catalyst with high conversion and selectivity reached superior space–time yields of carbon monoxide. At 500 °C, carbon monoxide production was twice that of Ni/Al_2O_3 with only half the hydrogen consumption.

The reaction mechanism involved in the rWGS reaction is still unclear. However, based on experimental and theoretical studies, two main routes were proposed: (i) via a redox mechanism[99–102] and (ii) via an associative route with formate as an intermediate.[103–106]

The surface redox mechanism involves the adsorption of CO_2 on the metallic active site and the oxidation of the active centres, leading to CO formation. In the following step, the metal sites are regenerated by reduction with H_2, forming water as a product.[107–109]

The associative mechanism involves hydrogen spillover on the metallic active site. The adsorption and activation of CO_2 are strongly support-dependent and can take place at the metallic site or the metal–support interface. After the formation of formate species as an intermediate, the reaction with the dissociated hydrogen leads to carbon monoxide and water as

products. Therefore, in contrast to the redox mechanism, CO is derived from the association of CO_2 with H_2.[110–113]

Even though CO_2 hydrogenation over nickel-supported catalysts have been extensively studied, there is not yet a broad consensus regarding the reaction mechanism. The major difference is related to the pathway of CO_2 activation, where the metal–support interface plays a key role.[7,114–118] For Ni/Al_2O_3 catalysts, it is assumed that CO and CH_4 are formed through formate species adsorbed on the support. Several authors proposed that CO_2 adsorbs and dissociates on metallic Ni^0 forming *CO species. Then, the migration onto alumina is followed by the formation of carbonates species. In the following step, carbonates react with the dissociated hydrogen leading to formate species as an intermediate. This mechanism was evidenced by in situ FT-IR experiments. The formates can be further hydrogenated forming CH_4, or desorbed leading to CO and H_2O.[23,119–121] Similarly, it was demonstrated for Cu/Al_2O_3 catalysts that the CO_2 hydrogenation reaction occurs via formates as an intermediate.[122–125]

Moreover, it is possible to rationalize the catalytic activity and selectivity of the different catalysts taking into account the different adsorption energies of the educts and products. By temperature programmed desorption studies, it is reported that carbon dioxide preferably adsorbs on Cu sites. Thus, the addition of Cu to Ni catalysts could promote the activity in CuNi alloys. As can be seen in Fig. 4a, carbon dioxide conversion in $Cu_{25}Ni_{75}/Al_2O_3$ is slightly superior to that in Ni/Al_2O_3. However, Cu-rich catalysts showed a lower performance, related to their low thermal stability and sintering of copper.[97,126]

On the other hand, the hydrogen adsorption capacity is higher on Ni catalysts; meanwhile Cu presents a low hydrogen adsorption capacity. In addition, carbon monoxide

480 | Catal. Sci. Technol., 2022, **12**, 474–487

This journal is © The Royal Society of Chemistry 2022

is preferentially adsorbed on Ni rather than on Cu sites.[127,128] Thus, Ni catalysts promote methanation due to the consecutive hydrogenation of carbon monoxide to methane.[32,34,129] Therefore, Cu maximizes the synergy between both metals, promoting CO desorption and suppressing methane formation.[24,36,130] Thus, the catalytic performance can be improved by promoting the close interaction between both metals, enhancing the carbon dioxide conversion and selectivity to carbon monoxide.

Particle size and elemental distribution of alloyed structures

HAADF-STEM combined with EDS mapping is a powerful technique for investigating the morphology and composition of the active sites in supported multimetallic nanostructured catalysts.

Before reaction, the fresh Ni/Al_2O_3 catalyst showed small and dispersed Ni nanoparticles of 5.2 ± 2.7 nm (Fig. 5 and S7†). After 30 h time on stream, the particle size just slightly increased showing a particle size distribution of 5.5 ± 1.9 nm.

Thus, Ni nanoparticles were preserved, in agreement with the high activity and stability of the catalyst (Fig. 6 and S8†). As stated by the XPS and H_2-TPR results, Ni nanoparticles are stabilized through the strong interaction with the Ni aluminate spinel phase, homogeneously dispersed on the support. In addition, small particles between 2 and 3 nm were detected on the spent catalyst (Fig. S8†). Therefore, a continuous reduction of the $NiAl_2O_4$ structure during the time on stream can be assumed for Ni/Al_2O_3, in agreement with the increment of the carbon monoxide selectivity. Indeed, it has been reported that the particle size of Ni nanoparticles has a prominent influence on the selectivity of the reaction. Small nanoparticles lead to CO formation, while the larger ones lead to the formation of CH_4.[113,131]

The fresh Cu/Al_2O_3 catalyst showed larger nanoparticles of 6.7 ± 2.1 nm (Fig. 5 and S9†). However, a clear sintering process took place after the reaction, forming large particles with a broad size distribution of 22.8 ± 12.9 nm (Fig. 6 and S10a†). In addition, particles up to 100 nm could be detected, in agreement with the lack of stability of supported Cu
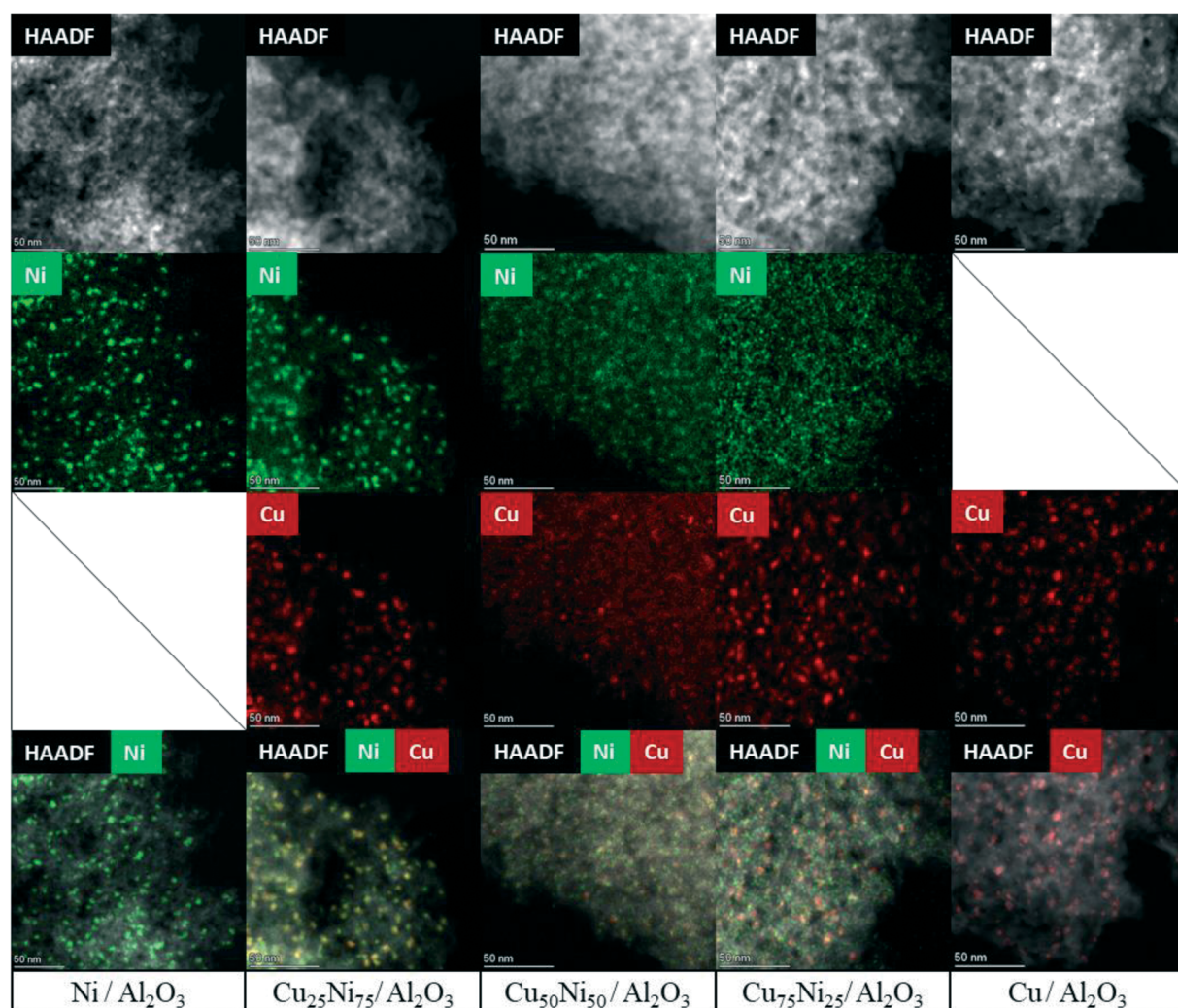

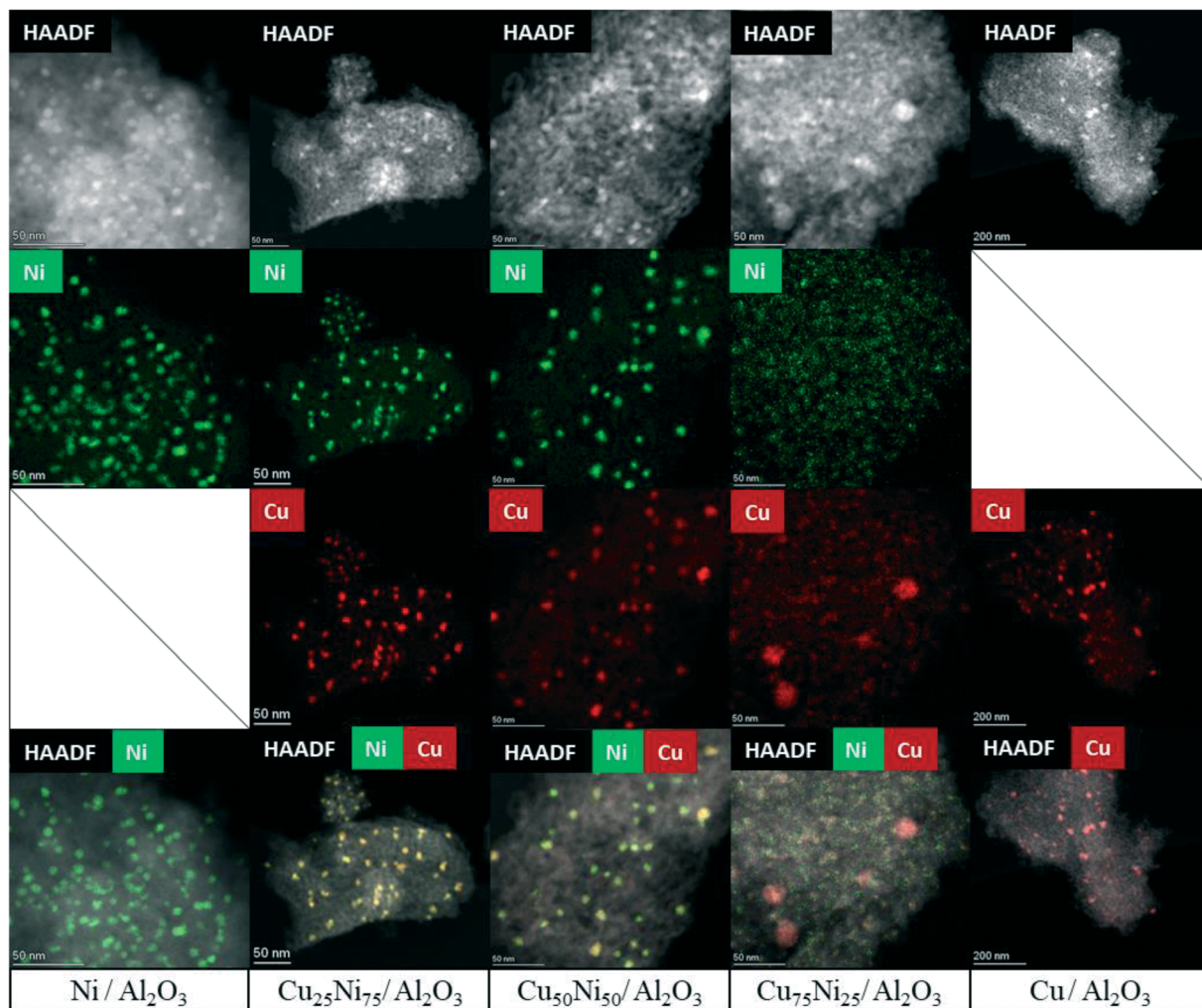Fig. 5 HAADF-STEM and EDS mapping of the fresh $CuNi/Al_2O_3$ catalysts.

This journal is © The Royal Society of Chemistry 2022

Catal. Sci. Technol., 2022, 12, 474–487 | 481

Fig. 6 HAADF-STEM and EDS mapping of the spent CuNi/Al$_2$O$_3$ catalysts.

catalysts (Fig. S10b†). Thus, the lower catalytic performance of Cu/Al$_2$O$_3$ is related to the migration and coalescence of the nanoparticles that significantly reduces the number of available active sites.[97]

The HAADF-STEM–EDS images of the fresh Cu$_{25}$Ni$_{75}$/Al$_2$O$_3$ catalyst are shown in Fig. 5. It can be clearly seen that Cu and Ni form small and dispersed alloyed nanoparticles of 4.5 ± 1.2 nm, with different Cu/Ni ratios (Fig. S11†). Notably, neither Ni nor Cu was detected as segregated particles. After 30 h time on stream, a slight sintering process led to the formation of particles of 8.4 ± 2.9 nm. Some isolated agglomerates up to 20 nm could be observed (Fig. S12†). Nevertheless, the nanoparticles remained alloyed instead of forming segregated Cu and Ni phases. The tendency of the nanoparticles to stay in the alloyed state can be rationalized by the similarity of Cu and Ni (same crystal structure fcc, similar atomic radii of 117 pm and 115 pm for Cu and Ni, respectively, valence of +1 and electronegativity of 1.90 and 1.91 by Pauling scale for Cu and Ni, respectively) which favours solid solutions of bot metals in the reduced state.[132,133] Thus, the outstanding performance of Cu$_{25}$Ni$_{75}$/Al$_2$O$_3$ is related to the formation of stable CuNi nanostructures (Fig. 7).

Considering the hydrogen consumption after reduction at 500 °C (Table S2†), Cu$_{25}$Ni$_{75}$/Al$_2$O$_3$ showed a reduction degree of 35%. Thus, the presence of the unreduced Ni spinel structure on the surface of the catalyst could be responsible for stabilizing the formed CuNi nanoalloys. A decrease in the carbon dioxide conversion during the ramping down is in agreement with the loss of the active surface area due to changes in the particle size. However, the preservation of the nanoalloy structure enhances the carbon monoxide selectivity, suppressing methane formation and leading to high CO yield during the 30 h of time on stream.

The fresh Cu$_{50}$Ni$_{50}$/Al$_2$O$_3$ catalyst showed an initial particle size distribution of 3.5 ± 1.6 nm, and similar to Cu$_{25}$Ni$_{75}$/Al$_2$O$_3$, Cu and Ni form alloyed structures with different Cu/Ni ratios (Fig. 5 and S13†). The small particle size is in agreement with the high initial catalytic activity. However, after the reaction the particle size increases to 10.3 ± 5.1 nm (Fig. 6 and S14a†). Moreover, alloyed particles up to 80 nm and a Cu/Ni ratio of 1 : 1 could be observed (Fig. S14b†). Thus, the sintering of the bimetallic CuNi alloys explains the deactivation. However, similar to Cu$_{25}$Ni$_{75}$/Al$_2$O$_3$ the particles remained alloyed after the reaction.
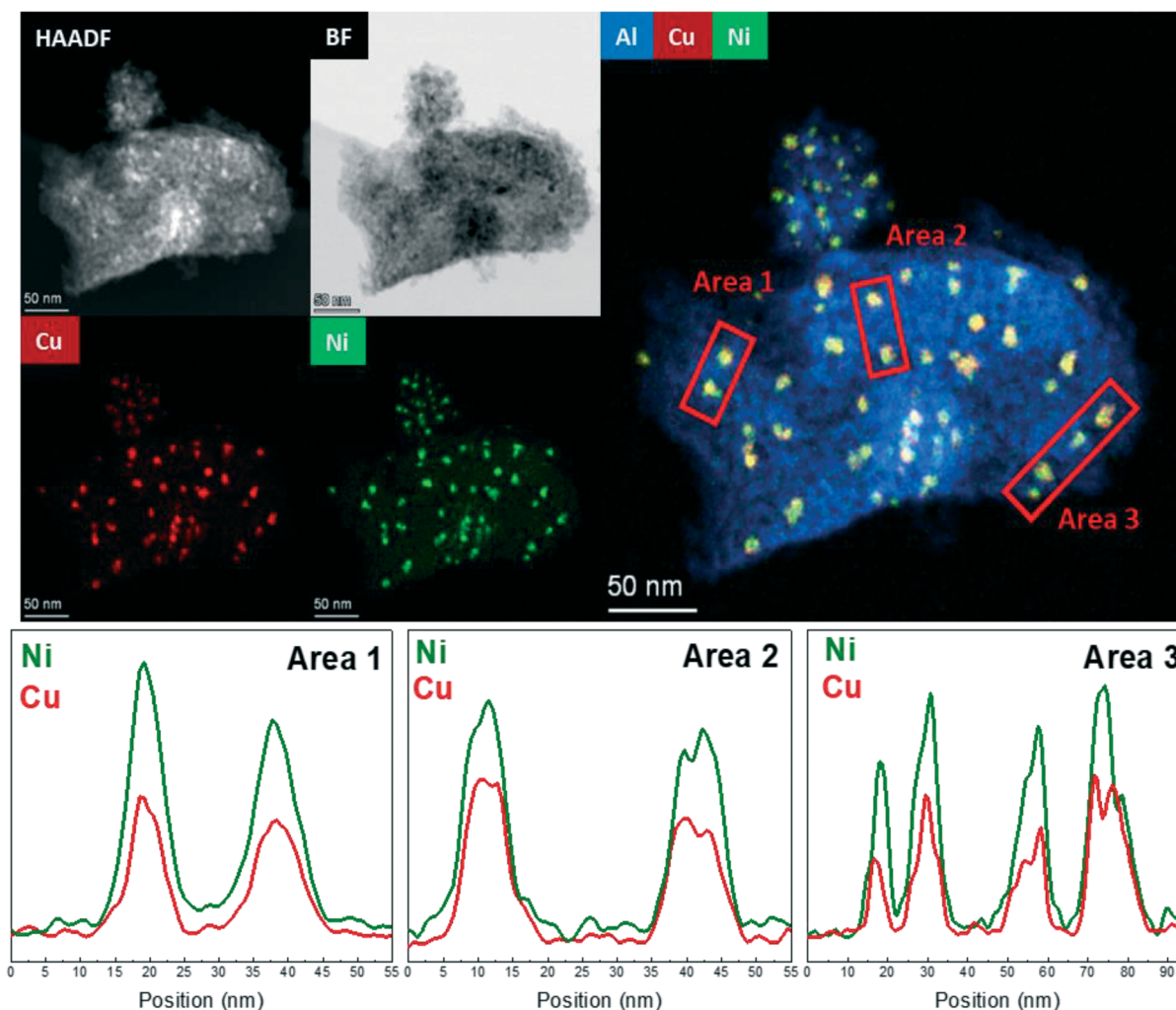
Fig. 7 HAADF-STEM and EDS mapping of $Cu_{25}Ni_{75}/Al_2O_3$ after 30 h time on stream.

The corresponding STEM–EDS images of fresh $Cu_{75}Ni_{25}/Al_2O_3$ can be seen in Fig. 5 and S15.† In contrast to $Cu_{25}Ni_{75}/Al_2O_3$ and $Cu_{50}Ni_{50}/Al_2O_3$, bimetallic CuNi alloyed nanoparticles could not be detected. In fact, the catalyst is formed by well-defined Cu nanoparticles of 5.5 ± 1.9 nm, while Ni species are uniformly dispersed on the support. After the reaction, $Cu_{75}Ni_{25}/Al_2O_3$ showed the formation of both alloyed Cu–Ni and large monometallic Cu nanoparticles up to 20–30 nm (Fig. 6 and S16a and b†). Despite the formation of bimetallic alloys, the high Cu content tends to form sintered Cu nanoparticles, with the consequent reduction of the active surface area. This is in agreement with the low catalytic performance and clear deactivation of $Cu_{75}Ni_{25}/Al_2O_3$.

Fig. S17† shows the particle size distribution of both fresh and spent $CuNi/Al_2O_3$ catalysts. In addition, elemental analysis of both fresh and spent catalysts was performed (Table S4†). As can be seen, the carbon content was very low and close to the quantification limit. Thus, the deactivation process of the catalysts is attributed to sintering of the active sites and loss of surface area, instead of deposition of carbonaceous species and coke formation.

In summary, small and dispersed Ni particles were formed after activation of the Ni/Al_2O_3 catalyst. The nanoparticles were highly stable after 30 h time on stream with no significant changes in the particle size, in close interaction with the unreduced Ni aluminate phase on alumina. $Cu_{75}Ni_{25}/Al_2O_3$ as the catalyst with the lowest Ni content is composed of defined Cu nanoparticles supported on Ni aluminate homogeneously distributed on the support. The close interaction between Cu and Ni promotes the reducibility of Ni species and the thermal stability of Cu nanoparticles, in comparison with the monometallic Cu/Al_2O_3. This is in agreement with the catalytic performance. However, the relatively high Cu content tends to form large agglomerates.

$Cu_{25}Ni_{75}/Al_2O_3$ and $Cu_{50}Ni_{50}/Al_2O_3$ evidenced the formation of dispersed alloyed nanoparticles. Despite the sintering after the reaction, the supported particles remained alloyed even after 30 h time on stream. Thus, Cu was incorporated in the Ni catalysts rather than forming separate phases, improving the thermal stability. The sintering was significantly larger for $Cu_{50}Ni_{50}/Al_2O_3$ than $Cu_{25}Ni_{75}/Al_2O_3$, in agreement with a higher

This journal is © The Royal Society of Chemistry 2022

Catal. Sci. Technol., 2022, **12**, 474–487 | **483**

Cu content. Regarding Ni-rich catalysts, the incorporation of Cu significantly enhances the catalytic performance through the formation of well-dispersed bimetallic CuNi alloyed structures. In addition, the formation of CuNi alloys in strong interaction with the support promotes thermal stability, especially for $Cu_{25}Ni_{75}/Al_2O_3$.[36,134]

Conclusions

Supported $CuNi/Al_2O_3$ catalysts were tested in the reverse water gas shift reaction. It was found that the reducibility of Ni is increased by the addition of Cu, and the nature of the formed bimetallic nanoparticles depends on the nominal Cu/Ni ratio.

Using Ni supported catalysts leads to methane formation through consecutive carbon monoxide hydrogenation. Meanwhile, Cu catalysts showed complete selectivity to carbon monoxide but low performance due to sintering and loss of active surface area.

For $Cu_{25}Ni_{75}/Al_2O_3$ the synergism between the thermal stability and bimetallic composition of the nanoparticles leads to better catalytic performance in terms of conversion and selectivity. CuNi alloyed nanoparticles maximize the synergy between both metals, promote the selectivity to carbon monoxide and suppress methane formation. Cu was incorporated in the Ni catalysts rather than forming separate phases, as was verified by HAADF-STEM EDS. In addition, $Cu_{25}Ni_{75}$ particles remained alloyed even after 30 h time on stream.

The incorporation of Cu into supported Ni catalysts is an excellent strategy to tune the electronic properties of the active metal, improving the selectivity to carbon monoxide through the formation of stable alloys and enhancing the performance in the reverse water gas shift reaction. Further studies should be conducted to improve the long-term stability of bimetallic nanoparticles under harsher reaction conditions.

Conflicts of interest

There are no conflicts to declare.

Acknowledgements

Notes and references

1 Y. Lu, P. Zhou, J. Han and F. Yu, *RSC Adv.*, 2015, **5**, 59792–59803.

2 D. X. Martínez-Vargas, L. Sandoval-Rangel, O. Campuzano-Calderon, M. Romero-Flores, F. J. Lozano, K. D. P. Nigam, A. Mendoza and A. Montesinos-Castellanos, *Ind. Eng. Chem. Res.*, 2019, **58**, 15872–15901.

3 F. Studt, M. Behrens, E. L. Kunkes, N. Thomas, S. Zander, A. Tarasov, J. Schumann, E. Frei, J. B. Varley, F. Abild-Pedersen, J. K. Nørskov and R. Schlögl, *ChemCatChem*, 2015, **7**, 1105–1111.

4 K. Wittich, M. Krämer, N. Bottke and S. A. Schunk, *ChemCatChem*, 2020, **12**, 2130–2147.

5 E. Schwab, A. Milanov, S. A. Schunk, A. Behrens and N. Schödel, *Chem. Ing. Tech.*, 2015, **87**, 347–353.

6 P. Ingale, C. Guan, R. Kraehnert, R. Naumann d'Alnoncourt, A. Thomas and F. Rosowski, *Catal. Today*, 2021, **362**, 47–54.

7 Y. A. Daza and J. N. Kuhn, *RSC Adv.*, 2016, **6**, 49675–49691.

8 J. Artz, T. E. Müller, K. Thenert, J. Kleinekorte, R. Meys, A. Sternberg, A. Bardow and W. Leitner, *Chem. Rev.*, 2018, **118**, 434–504.

9 W. Li, H. Wang, X. Jiang, J. Zhu, Z. Liu, X. Guo and C. Song, *RSC Adv.*, 2018, **8**, 7651–7669.

10 S. Dabral and T. Schaub, *Adv. Synth. Catal.*, 2019, **361**, 223–246.

11 R. Schlögl, *Top. Catal.*, 2016, **59**, 772–786.

12 L. Pastor-Pérez, F. Baibars, E. Le Sache, H. Arellano-García, S. Gu and T. R. Reina, *J. CO2 Util.*, 2017, **21**, 423–428.

13 E. Frei, A. Gaur, H. Lichtenberg, C. Heine, M. Friedrich, M. Greiner, T. Lunkenbein, J. Grunwaldt and R. Schlögl, *ChemCatChem*, 2019, **11**, 1587–1592.

14 S. Sourav and I. E. Wachs, *Catalysts*, 2020, **10**, 305–321.

15 M. Behrens and R. Schlögl, *Z. Anorg. Allg. Chem.*, 2013, **639**, 2683–2695.

16 C. J. Keturakis, M. Zhu, E. K. Gibson, M. Daturi, F. Tao, A. I. Frenkel and I. E. Wachs, *ACS Catal.*, 2016, **6**, 4786–4798.

17 T. Lunkenbein, J. Schumann, M. Behrens, R. Schlögl and M. G. Willinger, *Angew. Chem., Int. Ed.*, 2015, **54**, 4544–4548.

18 S. S. Kim, H. H. Lee and S. C. Hong, *Appl. Catal., A*, 2012, **423–424**, 100–107.

19 F. Sun, C. Yan, Z. Wang, C. Guo and S. Huang, *Int. J. Hydrogen Energy*, 2015, **40**, 15985–15993.

20 L. C. Wang, M. Tahvildar Khazaneh, D. Widmann and R. J. Behm, *J. Catal.*, 2013, **302**, 20–30.

21 R. Mutschler, E. Moioli, W. Luo, N. Gallandat and A. Züttel, *J. Catal.*, 2018, **366**, 139–149.

22 A. Wolf, A. Jess and C. Kern, *Chem. Eng. Technol.*, 2016, **39**, 1040–1048.

484 | *Catal. Sci. Technol.*, 2022, **12**, 474–487

This journal is © The Royal Society of Chemistry 2022

23 Z. Zhang, Y. Tian, L. Zhang, S. Hu, J. Xiang, Y. Wang, L. Xu, Q. Liu, S. Zhang and X. Hu, *Int. J. Hydrogen Energy*, 2019, **44**, 9291–9306.

24 J. Ashok, M. H. Wai and S. Kawi, *ChemCatChem*, 2018, **10**, 3927–3942.

25 A. I. Tsiotsias, N. D. Charisiou, I. V. Yentekakis and M. A. Goula, *Nanomaterials*, 2020, **11**, 28–62.

26 L. R. Winter, E. Gomez, B. Yan, S. Yao and J. G. Chen, *Appl. Catal., B*, 2018, **224**, 442–450.

27 Y. Wang, L. R. Winter, J. G. Chen and B. Yan, *Green Chem.*, 2021, **23**, 249–267.

28 S. Sengupta, A. Jha, P. Shende, R. Maskara and A. K. Das, *J. Environ. Chem. Eng.*, 2019, **7**, 102911.

29 L. Wang, H. Liu, Y. Chen and S. Yang, *Int. J. Hydrogen Energy*, 2017, **42**, 3682–3689.

30 J.-H. Lin, P. Biswas, V. V. Guliants and S. Misture, *Appl. Catal., A*, 2010, **387**, 87–94.

31 A. Jha, D.-W. Jeong, W.-J. Jang, C. V. Rode and H.-S. Roh, *RSC Adv.*, 2015, **5**, 1430–1437.

32 Y. Liu and D. Liu, *Int. J. Hydrogen Energy*, 1999, **24**, 351–354.

33 Y. R. Dias and O. W. Perez-Lopez, *Energy Convers. Manage.*, 2020, **203**, 112214–112223.

34 L. Deng, X. Ai, F. Xie and G. Zhou, *Chem. – Asian J.*, 2021, **16**, 949–958.

35 W. T. Figueiredo, C. Escudero, V. Pérez-Dieste, C. A. Ospina and F. Bernardi, *J. Phys. Chem. C*, 2020, **124**, 16868–16878.

36 L. X. Wang, E. Guan, Z. Wang, L. Wang, Z. Gong, Y. Cui, Z. Yang, C. Wang, J. Zhang, X. Meng, P. Hu, X. Q. Gong, B. C. Gates and F. S. Xiao, *ACS Catal.*, 2020, **10**, 9261–9270.

37 B. Lu, Y. Ju, T. Abe and K. Kawamoto, *Inorg. Chem. Front.*, 2015, **2**, 741–748.

38 D. L. Jurković, A. Pohar, V. D. B. C. Dasireddy and B. Likozar, *Chem. Eng. Technol.*, 2017, **40**, 973–980.

39 C.-S. Chen, W.-H. Cheng and S. Lin, *Appl. Catal., A*, 2004, **257**, 97–106.

40 J. R. A. Sietsma, A. Jos van Dillen, P. E. de Jongh and K. P. de Jong, in *Studies in Surface Science and Catalysis*, Elsevier Masson SAS, 2006, vol. 162, pp. 95–102.

41 D. Monti and A. Baiker, *J. Catal.*, 1983, **83**, 323–335.

42 J. R. A. Sietsma, H. Friedrich, A. Broersma, M. Versluijs-Helder, A. Jos van Dillen, P. E. de Jongh and K. P. de Jong, *J. Catal.*, 2008, **260**, 227–235.

43 B. C. Miranda, R. J. Chimentão, J. B. O. Santos, F. Gispert-Guirado, J. Llorca, F. Medina, F. L. Bonillo and J. E. Sueiras, *Appl. Catal., B*, 2014, **147**, 464–480.

44 A. Kumar, E. E. Wolf and A. S. Mukasyan, *AIChE J.*, 2011, **57**, 3473–3479.

45 W. M. Keely and H. W. Maynor, *J. Chem. Eng. Data*, 1963, **8**, 297–300.

46 P. Jeevanandam, Y. Koltypin and A. Gedanken, *Mater. Sci. Eng., B*, 2002, **90**, 125–132.

47 G. A. Naikoo, R. A. Dar and F. Khan, *J. Mater. Chem. A*, 2014, **2**, 11792–11798.

48 B. Małecka, A. Łącz, E. Drożdż and A. Małecki, *J. Therm. Anal. Calorim.*, 2015, **119**, 1053–1061.

49 J. Dong, J. Wang, L. Shi, J. Yang, J. Wang, B. Shan and M. Shen, *Phys. Chem. Chem. Phys.*, 2017, **19**, 27389–27396.

50 K. M. Parida, A. C. Pradhan, J. Das and N. Sahu, *Mater. Chem. Phys.*, 2009, **113**, 244–248.

51 A. Patel, P. Shukla, G. T. Pan, S. Chong, V. Rudolph and Z. Zhu, *J. Environ. Chem. Eng.*, 2017, **5**, 2350–2361.

52 W. Hu, F. Donat, S. A. Scott and J. S. Dennis, *RSC Adv.*, 2016, **6**, 113016–113024.

53 P. H. Bolt, F. H. P. M. Habraken and J. W. Geus, *J. Solid State Chem.*, 1998, **135**, 59–69.

54 J. Wu, Q. Xia, H. Wang and Z. Li, *Appl. Catal., B*, 2014, **156–157**, 265–272.

55 N. Kanjanasoontorn, T. Permsirivanich, T. Numpilai, T. Witoon, N. Chanlek, M. Niamlaem, C. Warakulwit and J. Limtrakul, *Catal. Lett.*, 2016, **146**, 1943–1955.

56 A. Devard, P. Brussino, F. A. Marchesini and M. A. Ulla, *J. Environ. Chem. Eng.*, 2019, **7**, 103201.

57 F. J. Mariño, E. G. Cerrella, S. Duhalde, M. Jobbagy and M. A. Laborde, *Int. J. Hydrogen Energy*, 1998, **23**, 1095–1101.

58 H. Wang, J.-Z. Xu, J.-J. Zhu and H.-Y. Chen, *J. Cryst. Growth*, 2002, **244**, 88–94.

59 J. L. Cuya Huaman, K. Sato, S. Kurita, T. Matsumoto and B. Jeyadevan, *J. Mater. Chem.*, 2011, **21**, 7062–7070.

60 W. Li, G. Fan, L. Yang and F. Li, *Green Chem.*, 2017, **19**, 4353–4363.

61 Y. S. Yun, D. S. Park and J. Yi, *Catal. Sci. Technol.*, 2014, **4**, 3191–3202.

62 Z. Wu, R. Ran, Y. Ma, X. Wu, Z. Si and D. Weng, *Res. Chem. Intermed.*, 2019, **45**, 1309–1325.

63 M. Romero-Sáez, A. B. Dongil, N. Benito, R. Espinoza-González, N. Escalona and F. Gracia, *Appl. Catal., B*, 2018, **237**, 817–825.

64 E. Gioria, F. Marchesini, A. Soldati, A. Giorello, J. Hueso and L. Gutierrez, *Appl. Sci.*, 2019, **9**, 4075–4092.

65 C. Hernández Mejía, J. E. S. van der Hoeven, P. E. de Jongh and K. P. de Jong, *ACS Catal.*, 2020, **10**, 7343–7354.

66 Z. Wang, H. Wan, B. Liu, X. Zhao, X. Li, H. Zhu, X. Xu, F. Ji, K. Sun, L. Dong and Y. Chen, *J. Colloid Interface Sci.*, 2008, **320**, 520–526.

67 S. J. Gentry and P. T. Walsh, *J. Chem. Soc., Faraday Trans. 1*, 1982, **78**, 1515.

68 M. Cai, J. Wen, W. Chu, X. Cheng and Z. Li, *J. Nat. Gas Chem.*, 2011, **20**, 318–324.

69 J. M. Jehng and C. M. Chen, *Catal. Lett.*, 2001, **77**, 147–154.

70 S. Srivastava, G. C. Jadeja and J. Parikh, *J. Mol. Catal. A: Chem.*, 2017, **426**, 244–256.

71 J. L. Ewbank, L. Kovarik, F. Z. Diallo and C. Sievers, *Appl. Catal., A*, 2015, **494**, 57–67.

72 L. Yu, M. Song, P. T. Williams and Y. Wei, *Ind. Eng. Chem. Res.*, 2019, **58**, 11770–11778.

73 D. E. Rivero-Mendoza, J. N. G. Stanley, J. Scott and K. F. Aguey-Zinsou, *Catalysts*, 2016, **6**, 170–185.

74 C. Jiménez-González, Z. Boukha, B. de Rivas, J. J. Delgado, M. Á. Cauqui, J. R. González-Velasco, J. I. Gutiérrez-Ortiz and R. López-Fonseca, *Appl. Catal., A*, 2013, **466**, 9–20.

This journal is © The Royal Society of Chemistry 2022

Catal. Sci. Technol., 2022, **12**, 474–487 | **485**

75 R. Yang, X. Li, J. Wu, X. Zhang and Z. Zhang, *J. Phys. Chem. C*, 2009, **113**, 17787–17794.

76 S. Weber, K. L. Abel, R. T. Zimmermann, X. Huang, J. Bremer, L. K. Rihko-Struckmann, D. Batey, S. Cipiccia, J. Titus, D. Poppitz, C. Kübel, K. Sundmacher, R. Gläser and T. L. Sheppard, *Catalysts*, 2020, **10**, 1471.

77 C. Li and Y.-W. Chen, *Thermochim. Acta*, 1995, **256**, 457–465.

78 A. R. Naghash, T. H. Etsell and S. Xu, *Chem. Mater.*, 2006, **18**, 2480–2488.

79 F. M. Berndt and O. W. Perez-Lopez, *React. Kinet., Mech. Catal.*, 2017, **120**, 181–193.

80 M. Kang, M. W. Song, T. W. Kim and K. L. Kim, *Can. J. Chem. Eng.*, 2002, **80**, 63–70.

81 M. Thommes, *Chem. Ing. Tech.*, 2010, **82**, 1059–1073.

82 M. Zhu, T. C. R. Rocha, T. Lunkenbein, A. Knop-Gericke, R. Schlögl and I. E. Wachs, *ACS Catal.*, 2016, **6**, 4455–4464.

83 G. Moretti, *Surf. Interface Anal.*, 1991, **17**, 745–750.

84 M. C. Biesinger, L. W. M. Lau, A. R. Gerson and R. S. C. Smart, *Appl. Surf. Sci.*, 2010, **257**, 887–898.

85 L. Lyu, L. Zhang, Q. Wang, Y. Nie and C. Hu, *Environ. Sci. Technol.*, 2015, **49**, 8639–8647.

86 M. A. Paviotti, L. A. Salazar Hoyos, V. Busilacchio, B. M. Faroldi and L. M. Cornaglia, *J. CO2 Util.*, 2020, **42**, 101328.

87 G. Garbarino, P. Riani, A. Infantes-Molina, E. Rodríguez-Castellón and G. Busca, *Appl. Catal., A*, 2016, **525**, 180–189.

88 A. Quindimil, U. De-La-Torre, B. Pereda-Ayo, A. Davó-Quiñonero, E. Bailón-García, D. Lozano-Castelló, J. A. González-Marcos, A. Bueno-López and J. R. González-Velasco, *Catal. Today*, 2020, **356**, 419–432.

89 P. G. Savva, K. Goundani, J. Vakros, K. Bourikas, C. Fountzoula, D. Vattis, A. Lycourghiotis and C. Kordulis, *Appl. Catal., B*, 2008, **79**, 199–207.

90 L. Xu, F. Wang, M. Chen, J. Zhang, K. Yuan, L. Wang, K. Wu, G. Xu and W. Chen, *RSC Adv.*, 2016, **6**, 28489–28499.

91 M.-M. Millet, G. Algara-Siller, S. Wrabetz, A. Mazheika, F. Girgsdies, D. Teschner, F. Seitz, A. Tarasov, S. V. Levchenko, R. Schlögl and E. Frei, *J. Am. Chem. Soc.*, 2019, **141**, 2451–2461.

92 E. Heracleous, A. Lee, K. Wilson and A. Lemonidou, *J. Catal.*, 2005, **231**, 159–171.

93 S. Danaci, L. Protasova, V. Middelkoop, N. Ray, M. Jouve, A. Bengaouer and P. Marty, *React. Chem. Eng.*, 2019, **4**, 1318–1330.

94 C. Jiménez-González, Z. Boukha, B. de Rivas, J. J. Delgado, M. Á. Cauqui, J. R. González-Velasco, J. I. Gutiérrez-Ortiz and R. López-Fonseca, *Appl. Catal., A*, 2013, **466**, 9–20.

95 L. Zhang, J. Lin and Y. Chen, *J. Chem. Soc., Faraday Trans.*, 1992, **88**, 497–502.

96 M. González-Castaño, B. Dorneanu and H. Arellano-García, *React. Chem. Eng.*, 2021, **6**, 954–976.

97 M. Li, A. Borsay, M. Dakhchoune, K. Zhao, W. Luo and A. Züttel, *Appl. Surf. Sci.*, 2020, **510**, 145439–145448.

98 Y. Yu, R. Jin, J. Easa, W. Lu, M. Yang, X. Liu, Y. Xing and Z. Shi, *Chem. Commun.*, 2019, **55**, 4178–4181.

99 G.-C. Wang and J. Nakamura, *J. Phys. Chem. Lett.*, 2010, **1**, 3053–3057.

100 S. Mine, T. Yamaguchi, K. W. Ting, Z. Maeno, S. M. A. H. Siddiki, K. Oshima, S. Satokawa, K. Shimizu and T. Toyao, *Catal. Sci. Technol.*, 2021, **11**, 4172–4180.

101 M.-A. Serrer, A. Gaur, J. Jelic, S. Weber, C. Fritsch, A. H. Clark, E. Saraçi, F. Studt and J.-D. Grunwaldt, *Catal. Sci. Technol.*, 2020, **10**, 7542–7554.

102 W. Lin, K. M. Stocker and G. C. Schatz, *J. Am. Chem. Soc.*, 2017, **139**, 4663–4666.

103 E. Vesselli, L. De Rogatis, X. Ding, A. Baraldi, L. Savio, L. Vattuone, M. Rocca, P. Fornasiero, M. Peressi, A. Baldereschi, R. Rosei and G. Comelli, *J. Am. Chem. Soc.*, 2008, **130**, 11417–11422.

104 S. Saeidi, S. Najari, F. Fazlollahi, M. K. Nikoo, F. Sefidkon, J. J. Klemeš and L. L. Baxter, *Renewable Sustainable Energy Rev.*, 2017, **80**, 1292–1311.

105 X. Chen, Y. Chen, C. Song, P. Ji, N. Wang, W. Wang and L. Cui, *Front. Chem.*, 2020, **8**, 1–21.

106 M. I. Alam, R. Cheula, G. Moroni, L. Nardi and M. Maestri, *Catal. Sci. Technol.*, 2021, **11**, 6601–6629.

107 M. A. A. Aziz, A. A. Jalil, S. Triwahyono and S. M. Sidik, *Appl. Catal., A*, 2014, **486**, 115–122.

108 M. J. L. Ginés, A. J. Marchi and C. R. Apesteguía, *Appl. Catal., A*, 1997, **154**, 155–171.

109 H. Jing, Q. Li, J. Wang, D. Liu and K. Wu, *J. Phys. Chem. C*, 2019, **123**, 1235–1251.

110 L. Yang, L. Pastor-Pérez, S. Gu, A. Sepúlveda-Escribano and T. R. Reina, *Appl. Catal., B*, 2018, **232**, 464–471.

111 Y. Zhang, L. Liang, Z. Chen, J. Wen, W. Zhong, S. Zou, M. Fu, L. Chen and D. Ye, *Appl. Surf. Sci.*, 2020, **516**, 146035.

112 A. Goguet, S. Shekhtman, R. Burch, C. Hardacre, F. Meunier and G. Yablonsky, *J. Catal.*, 2006, **237**, 102–110.

113 H. C. Wu, Y. C. Chang, J. H. Wu, J. H. Lin, I. K. Lin and C. S. Chen, *Catal. Sci. Technol.*, 2015, **5**, 4154–4163.

114 L. Shen, J. Xu, M. Zhu and Y.-F. Han, *ACS Catal.*, 2020, **10**, 14581–14591.

115 Q. Pan, J. Peng, T. Sun, S. Wang and S. Wang, *Catal. Commun.*, 2014, **45**, 74–78.

116 H. Muroyama, Y. Tsuda, T. Asakoshi, H. Masitah, T. Okanishi, T. Matsui and K. Eguchi, *J. Catal.*, 2016, **343**, 178–184.

117 N. M. Martin, F. Hemmingsson, A. Schaefer, M. Ek, L. R. Merte, U. Hejral, J. Gustafson, M. Skoglundh, A.-C. Dippel, O. Gutowski, M. Bauer and P.-A. Carlsson, *Catal. Sci. Technol.*, 2019, **9**, 1644–1653.

118 S. Jantarang, E. C. Lovell, T. H. Tan, B. Xie, J. Scott and R. Amal, *Catal. Sci. Technol.*, 2021, **11**, 5297–5309.

119 N. A. A. Fatah, A. A. Jalil, N. F. M. Salleh, M. Y. S. Hamid, Z. H. Hassan and M. G. M. Nawawi, *Int. J. Hydrogen Energy*, 2020, **45**, 18562–18573.

120 A. Cárdenas-Arenas, A. Quindimil, A. Davó-Quiñonero, E. Bailón-García, D. Lozano-Castelló, U. De-La-Torre, B. Pereda-Ayo, J. A. González-Marcos, J. R. González-Velasco and A. Bueno-López, *Appl. Catal., B*, 2020, **265**, 118538.

121 R. A. Hubble, J. Y. Lim and J. S. Dennis, *Faraday Discuss.*, 2016, **192**, 529–544.

486 | *Catal. Sci. Technol.*, 2022, **12**, 474–487

This journal is © The Royal Society of Chemistry 2022

122 A. M. Bahmanpour, F. Héroguel, M. Kılıç, C. J. Baranowski, L. Artiglia, U. Röthlisberger, J. S. Luterbacher and O. Kröcher, *ACS Catal.*, 2019, **9**, 6243–6251.

123 C. S. Chen, J. H. Wu and T. W. Lai, *J. Phys. Chem. C*, 2010, **114**, 15021–15028.

124 C.-S. Chen, W.-H. Cheng and S. Lin, *Catal. Lett.*, 2000, **68**, 45–48.

125 A. M. Bahmanpour, F. Héroguel, M. Kılıç, C. J. Baranowski, P. Schouwink, U. Röthlisberger, J. S. Luterbacher and O. Kröcher, *Appl. Catal., B*, 2020, **266**, 118669.

126 K. N. Papageridis, G. Siakavelas, N. D. Charisiou, D. G. Avraam, L. Tzounis, K. Kousi and M. A. Goula, *Fuel Process. Technol.*, 2016, **152**, 156–175.

127 R. Naumann d'Alnoncourt, M. Kurtz, H. Wilmer, E. Löffler, V. Hagen, J. Shen and M. Muhler, *J. Catal.*, 2003, **220**, 249–253.

128 A. Kitla, O. V. Safonova and K. Föttinger, *Catal. Lett.*, 2013, **143**, 517–530.

129 S. Choi, B.-I. Sang, J. Hong, K. J. Yoon, J.-W. Son, J.-H. Lee, B.-K. Kim and H. Kim, *Sci. Rep.*, 2017, **7**, 41207.

130 Z. Bian, S. Das, M. H. Wai, P. Hongmanorom and S. Kawi, *ChemPhysChem*, 2017, **18**, 3117–3134.

131 C.-S. Chen, C. S. Budi, H.-C. Wu, D. Saikia and H.-M. Kao, *ACS Catal.*, 2017, **7**, 8367–8381.

132 G. Guisbiers, S. Khanal, F. Ruiz-Zepeda, J. Roque de la Puente and M. José-Yacaman, *Nanoscale*, 2014, **6**, 14630–14635.

133 H. R. A. Ram, K. Venkatesh, K. Gopalakrishna, K. T. Kashyap and K. S. Sridhar, *J. Inst. Eng.: Ser. D*, 2019, **100**, 243–253.

134 H.-W. Chen, C.-Y. Wang, C.-H. Yu, L.-T. Tseng and P.-H. Liao, *Catal. Today*, 2004, **97**, 173–180.

This journal is © The Royal Society of Chemistry 2022

Catal. Sci. Technol., 2022, **12**, 474–487 | **487**